Theoretical and Experimental SHG Angular Intensity Patterns from Healthy and Proteolysed Muscles.

Denis Rouède, Jean-Jacques Bellanger, Emmanuel Schaub, Gaëlle Recher, François Tiaho

Theoretical and experimental SHG angular intensity patterns from healthy and proteolysed muscles.

AUTHORS

Denis Rouède,[†][*] Jean-Jacques Bellanger,[‡] Emmanuel Schaub,[§,¶] Gaëlle Recher,[‖] François Tiaho[§]

[†]Institut de Physique de Rennes, Département d'Optique, UMR UR1-CNRS 6251, [‡]Laboratoire Traitement du Signal et de l'Image, UMR UR1-INSERM U642, [§] IRSET, UMR UR1-INSERM U1085, Université de Rennes1, Campus de Beaulieu, 35042 Rennes CEDEX, France
[‖]Neurobiologie et développement, CNRS UPR 3294, 91198 Gif-Sur-Yvette CEDEX, France
*Correspondence: denis.rouede@univ-rennes1.fr

KEYWORDS

second harmonic generation microscopy; second harmonic scattering; skeletal muscle; mdx muscle

ABSTRACT

SHG angular intensity pattern (SHG-AIP) of healthy and proteolysed muscle tissues are simulated and imaged for the first time. The role of the spatial distribution of second order nonlinear emitters on SHG-AIP is highlighted. SHG-AIP with two symmetrical spots is found to be a signature of healthy muscle while SHG-AIP with one centered spot in pathological mdx muscle is found to be a signature of myofibrillar disorder. We also show that SHG-AIP provides information on the 3D structural organization of myofibrils in physiological and proteolysed muscle. Our results open a new avenue for future studies aimed at unraveling more complex physiological and pathological fibrillar tissues organization.

INTRODUCTION

Second Harmonic Generation (SHG) imaging microscopy (SHIM) has emerged as a powerful and non invasive technique for the study of fibrillar tissue possessing a second order nonlinear susceptibility $\chi^{(2)}$ (1,2). SHIM takes advantage of a nonlinear and coherent frequency-doubling optical effect that is inherent to very few biomolecules, i.e. collagen, myosin, tubulin that are packed in a non-centrosymmetric polycrystalline lattice. In SHIM experiments of biological tissue, phase matching between ω and 2ω waves cannot be fulfilled mainly due to i) optical dispersion ii) Gouy effect and iii) optical scattering. The main consequence is that coherence between harmonic waves is lost and that SHG intensity is reduced (3).

It is widely accepted that macroscopic organization of fibrils is a key factor influencing both intensity and angular emission of SHG signal that is often emitted in the forward direction but also in the backward one for selective periodic organization of nonlinear sources as demonstrated from different biological tissues (3-13). Theory of SHG emission anisotropy was first described in inorganic materials as second harmonic scattering (SHS) (14-17). Freund showed that selective spatial modulation of $\chi^{(2)}$ can act as a nonlinear diffraction

grating resulting in better coherence between harmonic waves leading to constructive interferences and to high SHG intensity in specific directions (14). Freund was the first to apply this theory to describe diffraction of harmonic optical radiation by collagen tissue. He showed that high SHG intensity can be obtained in directions fulfilling the following condition (14)

$$k_{2\omega} = 2k_{\omega} + Q. \qquad (1)$$

k_{ω} and $k_{2\omega}$ are respectively the wave vectors of fundamental and harmonic waves and Q is the wave vector associated to the spatial modulation of $\chi^{(2)}$. This equation, obtained for plane waves, has been described as the optical analog of x rays diffraction optical nonlinear Bragg's law. More recently, this theory has been extended to the high focusing limit (18,19). Tian et al. (20) theoretically demonstrated that collagen fibrils diameter, packing density and inter fibrils structure have a strong influence on SHG emission angle. In the case of a highly focused beam, we will show that direction of diffracted harmonic waves is determined by the following extension of Eq. 1

$$k_{2\omega} = 2\xi k_{\omega} + Q, \qquad (2)$$

where ξ is a coefficient that represents the effective reduction ($\xi < 1$) of k_{ω} due to Gouy effect (21-23).

In SHIM experiments, SHG signal is usually integrated through the NA of the collecting optic resulting in a loss of SHG-AIP and of most of the information relative to fibrillar organization. In the present work, we will first extend previous theoretical models (18-20,22) to calculate SHG-AIP in muscle tissue taking into account both the finite size of myofibrils, their polarity and the inhomogeneity of their distributions. We will next show that with small modification of the experimental set up, it is possible to obtain SHG intensity of healthy and proteolysed muscle tissues as a function of the forward angle of emission so as to deduce the forward SHG-AIP for each pixel of a scanned image. We find that healthy muscle with well aligned myofibrils is characterized by a unique SHG-AIP signature that is well predicted by the theoretical simulation. We also find that proteolysed muscle has more various SHG-AIPs that reveal more complex myofibrillar organization. In this work, which is to our knowledge the first report showing experimental SHG-AIPs of muscle tissue, we demonstrate that SHG-AIP technique provides extra hints to map at sub-optical resolution the 3D myofibrillar organization in both healthy and pathological conditions.

MATERIAL AND METHODS

Sample preparation

Muscle tissues were obtained from gastrocnemius of either adult *Xenopus laevis* (National breeding facility of xenopus animals in Rennes, France) or 6 months mouse. For xenopus, nine mature male animals were anesthetized by immersion for 10-15 min in 2% phenoxyethanol (Sigma-Aldrich) and divided into two groups of three animals each. The dissected gastrocnemius muscles were tied to rigid plastic rods after gentle stretching to 130% of resting length during pre and post fixation protocols. Muscle of the control group were immediately incubated in Mark's modified Ringer (MMR) solution containing 4%

paraformaldehyde (PFA) fixative whereas the muscles of proteolysed group experienced either 3 hours (mild proteolysis) or 6 hours *post-mortem* spontaneous proteolysis in MMR solution at room temperature (18-22°C) and then incubated in 4% PFA-MMR fixative. For mouse, gastrocnemius muscles of six wild type (BL10) and six mdx (mouse model of Duchenne muscular dystrophy) animals provided by Pr. Y. Cherel (ENV, ONIRIS, Nantes, France) were dissected in phosphate buffer saline (PBS). They were immediately fixed with 4 % PFA-PBS at slack length. For both xenopus and mouse, muscles were kept overnight at 4° C in the fixative and washed several times in the appropriate buffer saline. The immediate fixative procedure was previously shown to prevent spontaneous muscle proteolysis (24). Dissected pieces (200 - 400 µm thickness) of muscle fibers were mounted in a POC-R2 tissue culture chamber system (POC chamber system, PeCon, GmbH), in MMR or PBS and stabilized between two coverslips. Myofibrils were isolated according to previously described protocol. Briefly, pre-fixed muscles were cut into few millimeters wide strips and washed several times in ice-cold MMR solution. Muscle strips were then transferred in ice-cold rigor solution containing 50 mM KCl, 2 mM MgCl2, 10 mM imidazole-HCl, 2 mM EGTA-KOH, pH 7.4, 0.5 mM DTT, 0.1 mM PMSF. Samples were homogenized in this solution for 15 s with an Ultra-Turrax T25 homogeniser at medium speed (IKA Blue Line T25 Grosseron, Saint-Herblain, France). The pellet was collected by centrifugation at 4000 g, for 10 min at 4°C, and washed in the same ice-cold solution. This operation was repeated three times. 100 µl of the suspended sample was laid between two coverslips in the POC-R2 tissue culture chamber containing MMR.

SHG imaging system

SHG images were acquired on PIXEL (http://pixel.univ-rennes1.fr/) (facility of GIS EUROPIA, University of Rennes1, France). The SHG imaging system consists in a confocal Leica TCS SP2 scanning head (Leica Microsystems, Mannheim, Germany) mounted on a Leica DMIRE2 inverted microscope and equipped with a MAITAI Spectra Physics femtosecond laser (Spectra Physics, Santa Clara, CA, USA). High NA water immersion objective (Olympus LUMFL 60W × 1.1 NA) (Olympus, Tokyo, Japan) was used for applying 10-20 mW of 940 nm excitation at the sample. SHG signal was collected in forward direction using a water immersion condenser (Leica S1 NA=0.9-1.4). BG39 bandpass and 470 nm IR (10 nm FWHM) filters were placed before the PMT. All specimens were positioned on the fixed x, y stage of the microscope with polarization of the incident laser beam along y direction. In order to obtain SHG-AIP of each scanned image, the aperture diaphragm was removed from the condenser and replaced by a movable dark screen with a pinhole (See Fig. 1). A motorized xy stage was used to move the pinhole over the entire field of the aperture diaphragm. SHG images of the same field of view were obtained for P×P positions of the pinhole in order to map the entire field of the condenser aperture. Centering of the pinhole corresponding to θ = 0°, with an accuracy estimated to ±1°, was made before each experiment. Open source ImageJ software (http://rsb.info.nih.gov/ij/) was used to compute the average intensity within a particular ROI for the P×P images. MATLAB (MathWorks, Natick, MA, USA) was used to plot the corresponding experimental SHG-AIP.

SHG pattern quantification and ROC analysis

Sarcomeric SHG intensity pattern (SHG-IP) as previously reported (25) and SHG-AIP were quantified from muscle fibers of twelve animals (6 BL10, 6 mdx). For each animal five

random fields (60×60 μm) were selected. For each field, paired SHG-IP and SHG-AIP analysis were performed from height homogeneously distributed ROIs in the entire field. For SHG-IP, ROIs are full lines along myofibrils. For SHG-AIP, the ROI size is 7.5×60 μm. Student T-test (excel software), Receiver operating characteristic curve (ROC curve) and area under curve (ROC AUC) analysis were performed as previously reported by Plotnikov et al. (26) using SigmaPlot (Systat Software, San Jose, CA, USA).

THEORETICAL MODELING

A thorough theoretical study of SHG emission from fibrillar collagen has been done recently and it has been shown that both distribution of fibrils inside the fiber and focusing conditions are key factors influencing SHG emission angle (19,20). It is also known that shape and size of the biological tissue can also affect SHG signal. For example, when size of the sample is of the order of the optical wavelength, optical diffraction is significant and needs to be taken into account in the calculation of the SHG intensity. To correctly interpret experimental SHG-AIPs of muscle tissue, we have thus extended previous theoretical models (18-20,22) taking into account both polarity, size and distribution of myofibrils.
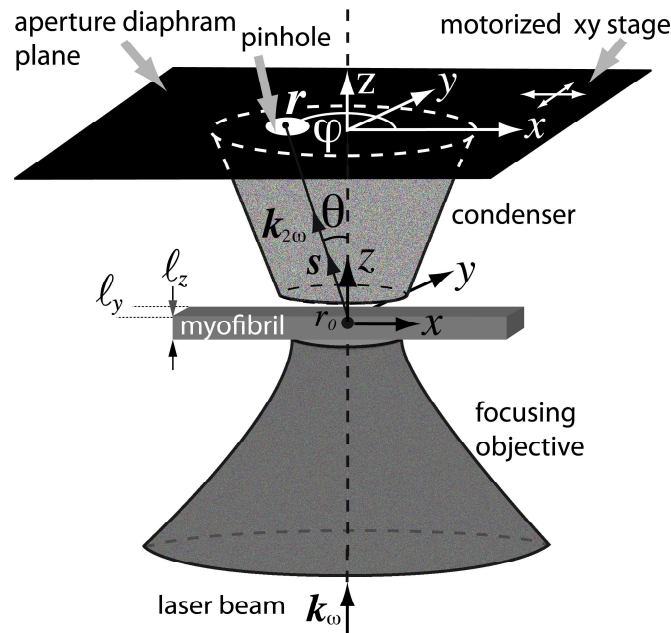

FIGURE 1. Schematic of the experiment. Excitation IR laser beam is propagating in z direction and is focused at x = y = z = 0. A pinhole is inserted in the plane of the aperture diaphragm to select a particular angle of SHG light emission. Forward SHG-AIP is obtained after acquisition of an image for each position of the pinhole that is moved by a motorized stage over the entire field of the aperture diaphragm (θ ~ 42.6°, NA=0.9).

Laser beam with incident wave vector $\mathbf{k}_\omega$ is chosen to propagate along z direction and is focused with high NA objective on a myofibril (see Fig. 1). Assuming that the excitation volume is 3D Gaussian at the vicinity of the focus, SHG intensity that is radiated in direction $\mathbf{r}(r,\theta,\varphi)$ is given in the far-field approximation, by (18,22,27)

$$I^{2\omega}(\boldsymbol{r}) = \frac{\omega^4}{r^2 c^4} \times P(\theta,\varphi)$$

$$\times \left| \int e^{-i\,\boldsymbol{k}_{2\omega}(\boldsymbol{r})\cdot\,\boldsymbol{r}_0}\, M(\boldsymbol{r}_0)\, e^{-2\frac{x_0^2+y_0^2}{w_{xy}^2}-2\frac{z_0^2}{w_z^2}+2i\xi k_\omega z_0}\, d^3\boldsymbol{r}_0 \right|^2 \qquad (3)$$

where summation is made over all nonlinear sources $\boldsymbol{r}_0$. Beam waist w_{xy} and w_z are obtained from the two-photon excitation PSF. $\xi = 1-(k_\omega\, z_r)^{-1}$ is a coefficient whose value is driven by the Rayleigh range $z_r = \pi n_\omega w_{xy}^2 \lambda_\omega^{-1}$. ξ represents the reduction ($\xi < 1$) of the effective axial propagation vector $\boldsymbol{k}_\omega$ caused by the phase anomaly or Gouy shift (21-23). $M(\boldsymbol{r}_0)$ is a modulation function that is introduced to take into account the spatial modulation of $\chi^{(2)}(\boldsymbol{r}_0)$. It is defined as follows $\chi^{(2)}(\boldsymbol{r}_0) = M(\boldsymbol{r}_0)\,\chi^{(2)}$ where $\chi^{(2)}$ is the uniform nonlinear susceptibility tensor. $P(\theta,\varphi) = \left|(I-\boldsymbol{ss})\chi^{(2)}\boldsymbol{E}^\omega\boldsymbol{E}^\omega\right|^2$ is a projection operator that represents the angular dependence of the radiation of each nonlinear dipole. I is the unity tensor, $\boldsymbol{s}$ is the unitary vector along $\boldsymbol{k}_{2\omega}$ and $\boldsymbol{E}^\omega$ is the electric field strength at the center point of the focused beam. To obtain simple analytical expressions, we consider that the myofibril is rectangular with size ℓ_y, ℓ_z respectively along y and z directions (see Fig. 1). In these conditions, $M(\boldsymbol{r}_0)$ is a periodical function in x direction with a period L_x equals to the sarcomere width and is an uniform function in y and z directions such that $M(\boldsymbol{r}_0)$ is factorizable

$$M(\boldsymbol{r}_0) = M_x(x_0) \times M_y(y_0) \times M_z(z_0). \qquad (4)$$

$M_y = M_z = 1$ within the myofibril and $M_y = M_z = 0$ elsewhere. $M_x = +1$ or -1 in the A-band region of each sarcomere and $M_x = 0$ elsewhere. The sign inversion takes into account myosin thick filament polarity inversion at the center of each sarcomere. As the myofibril has a finite transversal size, we can repeat it in y and z directions with spatial periods respectively equal to L_y and L_z. In order to have no influence on the result of the SHG intensity, L_y and L_z have to be chosen much larger than the laser focus spot that is the active volume to produce the SHG signal. Doing so, we can expand each coefficient M_η (η = x, y, z) in Fourier series (22)

$$M_\eta(\eta_0) = \sum_{n\in\mathbb{Z}} c_{\eta n}\, e^{jG_{\eta n}\eta_o}, \qquad (5)$$

with wave vector component $G_{\eta n}$ and Fourier coefficient $c_{\eta n}$ of order n given by

$$G_{\eta n} = 2\pi n L_\eta^{-1},$$

$$c_{\eta n} = L_\eta^{-1} \int_{-L_\eta/2}^{L_\eta/2} M_\eta(\eta_0) e^{-iG_{\eta n}\eta_0}\, d\eta_0. \qquad (6)$$

After straightforward calculation, using standard properties of Fourier transform, Eq. 3 results in

$$I^{2\omega}(\boldsymbol{r}) = \frac{\omega^4}{r^2 c^4}\left(\frac{\pi}{2}\right)^{3/2} w_{xy}^4 w_z^2 \, P(\theta,\varphi)\, |g(\theta,\varphi)|^2 \qquad (7)$$

with

$$
\begin{aligned}
g(\theta,\varphi) = &\sum_{n\in\square} c_{xn} e^{-\frac{1}{8}w_{xy}^2 \left(k_{2\omega}\sin\theta\cos\varphi - G_{xn}\right)^2} \\
&\times \sum_{n\in\square} c_{yn} e^{-\frac{1}{8}w_{xy}^2 \left(k_{2\omega}\sin\theta\sin\varphi - G_{yn}\right)^2} \\
&\times \sum_{n\in\square} c_{zn} e^{-\frac{1}{8}w_z^2 \left(k_{2\omega}\cos\theta - 2\xi k^{\omega} - G_{zn}\right)^2}.
\end{aligned}
$$

$$(8)$$

Fourier coefficients $c_{\eta n}$ are (22)

$$
\begin{aligned}
c_{xn} &= \tfrac{-2i}{\pi n}\sin^2(\tfrac{1}{4}G_{xn}\ell_x)\ \times \exp(-i G_{xn}\Delta_x)\,, \\
c_{y,zn} &= \tfrac{1}{\pi n}\sin(\tfrac{1}{2}G_{y,zn}\ell_{y,z})\times\exp(-i G_{y,zn}\Delta_{y,z})
\end{aligned}
$$

$$(9)$$

for $n \neq 0$ and $c_{xn} = 0$, $c_{yn} = \ell_y L_y^{-1}$, $c_{zn} = \ell_z L_z^{-1}$ for $n = 0$. ℓ_x is the width of the A-band region of each sarcomere. We also consider that thick filaments of each A-band are centered and perfectly aligned within each sarcomere. The effect of the antiparallel overlapping of myosin tails at the center of each sarcomere (M-band) is also neglected. Δ_x, Δ_y and Δ_z are coefficients that are introduced to take into account a possible displacement of the center of the sarcomere with respect to the focus spot in respectively x, y and z directions. This result can be generalized to identical adjacent bundle of myofibrils with possible different displacements Δ_η (η = x, y, z) relative to the center of the focus spot. In that case, $g(\theta,\varphi)$ is replaced by $\sum_f g^f(\theta,\varphi)$ in Eq. 7 where summation has to be done over all myofibrils f. $g^f(\theta,\varphi)$ is still given by Eq. 8 replacing $c_{\eta n}$ by $c_{\eta n}^f$ and $G_{\eta n}$ by $G_{\eta n}^f$ for each myofibril f. Finally, the total SHG intensity $I_T^{2\omega}$ collected by the condenser is obtained by angular integration of Eq. 7 over the condenser aperture

$$I_T^{2\omega} = \int I^{2\omega}(\boldsymbol{r})\, d\Omega\,, \qquad (10)$$

with $d\Omega = \sin\theta\, d\theta\, d\varphi$ the differential solid angle in spherical coordinates r, θ, φ. It is worth noting that if there is a dominant term in each sum of Eq. 8 corresponding to a unique $\boldsymbol{G}$, $g(\theta,\varphi)$ is maximum if $\boldsymbol{k}_{2\omega} = 2\xi\boldsymbol{k}_\omega + \boldsymbol{G}$. That corresponds to Eq. 2 with $\boldsymbol{G} = \boldsymbol{Q}$.

MATLAB (MathWorks, Natick, MA, USA) was used for the simulation of the radiated SHG intensity $I^{2\omega}(\boldsymbol{r})$. Choice of spatial periods L_x, L_y and L_z in the Fourier development serie is done such that $\left|\int_{|\eta|>\frac{L_\eta}{2}} e^{-2\eta^2 w_\eta^2}\, d\eta\right|^2 / \left|\int_{\square} e^{-2\eta^2 w_\eta^2}\, d\eta\right|^2 \ll 1$ where $w_\eta = w_{xy}$ and $w_\eta = w_z$ for respectively $\square\square\eta\square\square\square$ x or y and $\square\eta\square\square\square\square\square$ z. Condition to ensure that this ratio is less than 0.5 % gives $L_\eta \geq 1.81 \times w_\eta$ according to standard properties of the

cumulative distribution function of the Gaussian distribution (28). It is worth to note that SHG signal is only defined by the specific organization of myofibrils within a small focusing volume $(1.81)^3 \times w_{xy}^2 \times w_z = 3.3 \ \mu m^3$ of the order of the PSF. We have checked that the result of the theoretical simulation does not depend on the choice of L_η as long as the above condition is satisfied. For simplicity, we choose $L_y = L_z = 15 \ \mu m$ that are greater than the size of the bundle of myofibrils used in the simulation both in y and z directions. $L_x = 3 \ \mu m$ corresponds to the experimental average sarcomere width and also satisfies previous condition. Number of Fourier coefficients is set to 40 such that $I_T^{2\omega}$ is greater than 99 % of its limiting value. For all simulations, $\ell_y = \ell_z = 1 \ \mu m$, $\ell_x = 1.6 \ \mu m$ and refractive indices at fundamental and harmonic frequencies are taken equal $n_\omega = n_{2\omega} = 1.33$ (22). w_{xy} and w_z were estimated from the two-photon excitation point spread function obtained from 0.17 μm diameter fluorescent micro beads (Molecular Probes PS-Speck Microscope Point Source Kit (P7220)). Lateral and axial FWHM were found to be $\mathrm{FWHM}_{x,y} = 0.4 \ \mu m$ and $\mathrm{FWHM}_z = 2 \ \mu m$ at 940 nm. $w_{xy} = 0.48 \ \mu m$ and $w_z = 2.4 \ \mu m$ were deduced from these values using $w_{xy,z} = \mathrm{FWHM}_{xy,z} / \sqrt{\ln 2}$ (2,22). We have checked experimentally that $P(\theta, \varphi)$, whose value is driven by the polarization of the incident IR laser beam, is a parameter that does not change the shape of the SHG-AIP (see Fig. S1). It will therefore not be taking into account in the simulation.

Theoretical SHG-AIPs of sarcomeres from N×N adjacent myofibrils with different relative positions are shown in Fig. 2 as a function of N for both healthy (Fig. 2, *A* and *B*) and proteolysed muscles (Fig. 2, *C-G*). Only one sarcomeric A-band is shown for each myofibril and polarity inversion of myosin molecules at the center of the sarcomere is indicated with a different *red* (+1) and *blue* (-1) *color*. Based on our previous studies (22,25), we consider that adjacent sarcomeric A-bands of the N×N adjacent myofibrils are well aligned in healthy muscles (Fig. 2, *A* and *B*) and misaligned in proteolysed muscles (Fig. 2, *C-G*).
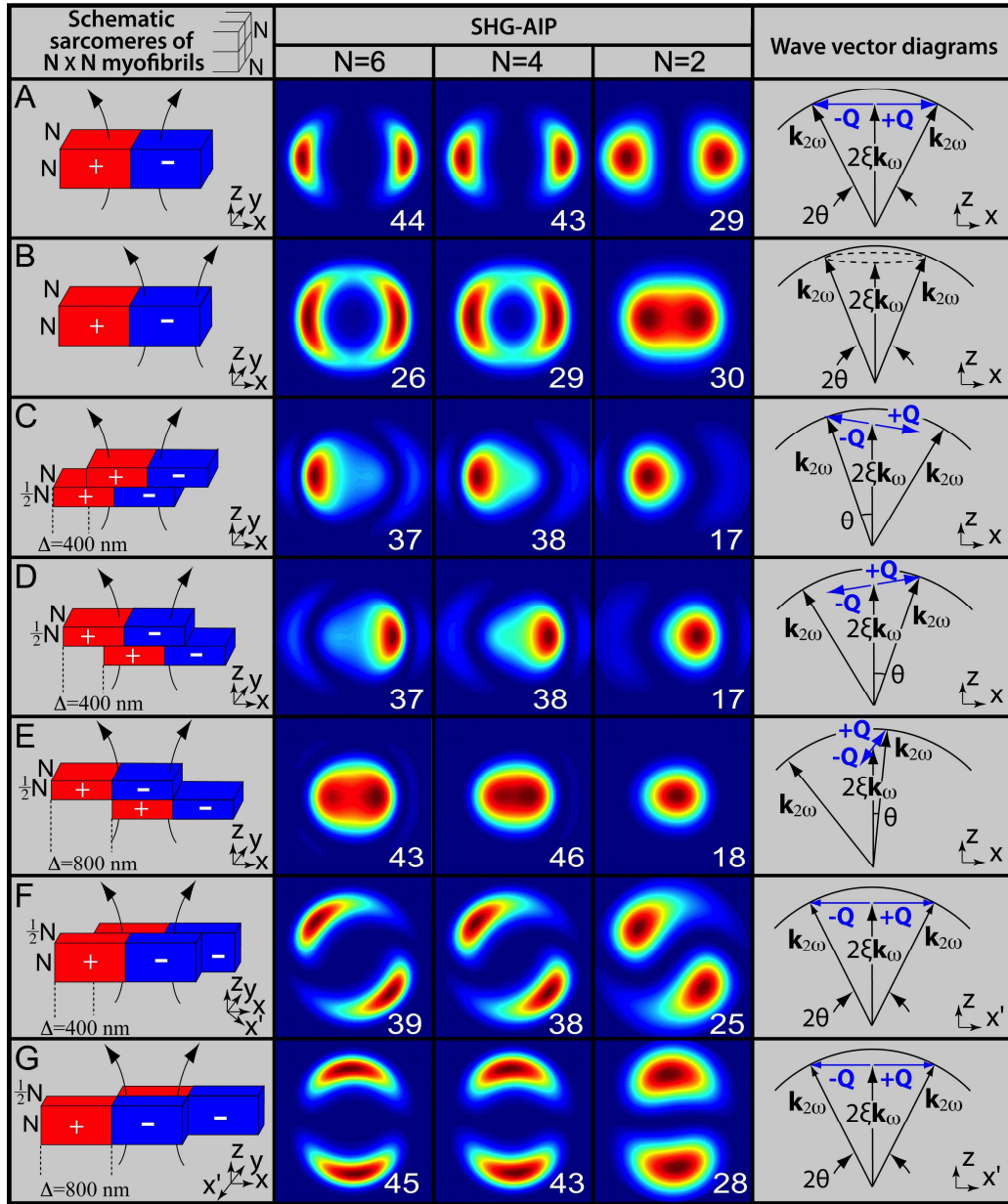
FIGURE 2. Theoretical SHG-AIPs and wave vector diagrams for sarcomeres of N×N adjacent myofibrils. The schematic diagram, its corresponding SHG-AIP and wave vector diagram are shown from left to right for each simulation as indicated by column titles. Each sarcomere consists of a centered A-band formed by thick filaments with polarity transition of myosin molecules indicated with a different *red* (+1) and *blue* (-1) *color*. All thick filaments are supposed to be centered and well aligned in each sarcomere. The focusing region is shown in each schematic diagram. Each SHG-AIP is represented in the xy plane with a full scale corresponding to -40° +40° in x and y directions with normalized increasing intensity ranging from 0 (*blue*) to 1 (*red*). Note that the value (relative units) of the SHG intensity corresponding to integration over the entire image is also shown in each SHG-AIP. (A) Case of a laser beam at the center of all aligned sarcomeric A-bands. (B) Case of a laser beam at the center of the hemi sarcomere. (C-E) Case of misaligned myofibrils in the xz plane. Wave vector modulation Q rotates from x to z direction for increasing values of $\Delta = \Delta_x/2$. (F-G) Case of misaligned myofibrils in the xy plane. Wave vector modulation Q is along x' direction and rotates from x to (-y) direction for increasing values of $\Delta = \Delta_x/2$. For all

simulations, myofibrils have identical thickness $\ell_y = \ell_z = 1\ \mu m$, $L_x = 3\ \mu m$, $L_y = L_z = 15\ \mu m$ and size of A-band is $\ell_x = 1.6\ \mu m$ (22). □Angle θ that is shown in each wave vector diagram indicates the direction of maximum SHG intensity.

For healthy muscle, when the laser beam is at the center of the sarcomere (Fig. 2 *A*), where A-bands thick filaments show polarity inversion, SHG-AIP exhibits two spots of equal intensity aligned along the main fiber axis and symmetrically located from z = 0 as previously reported (22). Maximum SHG intensity is obtained for $\theta = 26°$, $\theta = 25.6°$ and $\theta = 23°$ for respectively N=6, N=4 and N=2. Such anisotropy of emission can be explained as follows. If we consider that SHG signal is built in x direction over the elementary distance $1.81 \times w_{xy}$, polarity inversion occurring over such distance induces a spatial modulation of the nonlinear susceptibility with a dominant modulation wave vector component $Q_x = 2\pi / (1.81 \times w_{xy}) = 7.2\ \mu m^{-1}$ as $M_x(x_0)\exp(-2x_0^2 / w_{xy}^2)$ can be roughly approximated by $\sin(Q_x x_0)\exp(-2x_0^2 / w_{xy}^2)$ for $|x_0| \le \frac{1}{2}(1.81 \times w_{xy})$. Q_x is close to $\sqrt{k_{2\omega}^2 - 4\xi^2 k_\omega^2}$ $(= 8.1\ \mu m^{-1})$, the necessary modulation wave vector achieving Eq. 2. This result is schematized by the wave vector diagram in the last column of Fig. 2 *A*. For N=6, angle of emission $\theta = 26°$ of maximum SHG intensity is close to the Gouy angle $\cos^{-1}\xi = 27.1°$ demonstrating that Eq. 2 is achieved in that case. The slight decrease of θ for decreasing value of N is due to additional contribution of modulation wave vector with z component (Q_z) owing to optical diffraction. When the laser beam is at the center of the hemi A-band where polarity is uniform (Fig. 2 *B*), SHG-AIP presents an annular shape with two highlighted spots. Distance between these spots decreases with N and SHG-AIP is almost one centered spot for N=2. For N=4 and N=6, integrated SHG intensity (shown in each SHG-AIP thumbnail) is lower than in Fig. 2 *A* indicating that Eq. 2 is not satisfied in that case as $\boldsymbol{Q} = 0$.

SHG-AIPs of proteolysed muscle are also shown in Fig. 2 for different cases of myofibrillar misalignments. For misaligned myofibrils in the xz plane (Fig. 2, *C-E*), SHG-AIP has asymmetric spots with different intensities. For increasing value of misalignment $\Delta = 2\Delta_x$, the spot with the strongest intensity moves toward the center while the other moves away. SHG-AIP becomes one centered spot for $\Delta = 800\ nm$. We found that (data not shown) theoretical SHG-AIP is sensitive to myofibrillar misalignment below the optical resolution (< 200 nm). For N=4 and N=6, despite the apparent centrosymmetry along z direction due to polarity inversion, integrated SHG intensity is similar to that of Fig. 2 *A* suggesting that Eq. 2 remains satisfied. Indeed, when Δ is non-zero, a z component (Q_z) of the modulation wave vector $\boldsymbol{Q}$ is induced. In consequence, $\boldsymbol{Q}$ rotates from x to z when Δ varies from 0 to 800 nm. As illustrated in the wave vector diagrams, Eq. 2 is better satisfied for the spot that is close to the center. For $\Delta = 800\ nm$, $Q_x = 0$ and $Q_z = 2\pi / (1.81 \times w_z) = 1.4\ \mu m^{-1}$ which is approximately $|k_{2\omega} - 2\xi k_\omega| = 1.9\ \mu m^{-1}$, the necessary modulation wave vector achieving Eq. 2 in that case. For misaligned myofibrils in the xy plane (Fig. 2, *F* and *G*), SHG-AIP exhibits two spots of equal intensity. Direction of the two spots rotates from x to y direction when Δ increases from 0 (Fig. 2, *A*) to 800 nm (Fig. 2, *G*). In the later case, the dominant modulation wave vector $\boldsymbol{Q}$ is along y direction and the SHG-AIP is similar to that of Fig. 2 *A* with a rotation of 90°. Integrated SHG intensity is also unchanged suggesting that Eq. 2 remains satisfied as illustrated in the wave vector diagrams.

The main results of the theoretical analysis can be summarized as follows i) for healthy muscle tissue, SHG-AIP signature is two symmetrical spots along the myofibril main axis. High SHG intensity is obtained at the center of the sarcomere because Eq. 2 is satisfied due to polarity inversion ii) for proteolysed muscle tissue, despite the apparent centrosymmetry induced by the myofibrillar misalignment, integrated SHG intensity over the SHG-AIP is comparable to that of healthy muscle tissue for a laser beam at the center of the sarcomere, suggesting that Eq. 2 remains satisfied iii) shape of the SHG-AIP is also determined by direction and amplitude of the myofibrillar misalignment. These theoretical simulations therefore provide a framework to analyze in the following section, experimental SHG-AIP results obtained from healthy and proteolysed xenopus and mouse muscles.

EXPERIMENTAL RESULTS

For healthy muscles, SHG images and experimental SHG-AIPs are shown in Fig. 3 for thick tissue (Fig. 3 A), bundle of myofibrils (Fig. 3 B) and isolated myofibril (Fig. 3 C). SHG intensity patterns exhibit the usual regular bright single-band SHG intensity pattern (SHG-IP) mapping the periodical sarcomeric distribution of myosin thick filaments both in thick tissue (Fig. 3 A) and bundle of myofibrils (Fig. 3 B) as previously reported (24). For thick tissue, transversal views (Fig. 3 A) show that all sarcomeres are well registered at Z lines (xz section, bottom) and individual myofibrils cannot be resolved (yz section, right). SHG-AIPs of thick muscle tissue, bundle of myofibrils and isolated myofibrils from the entire fields always exhibit two distinguishable spots emitted along the myofibril main axis (Fig. 3 D, thumbnails A0, B0, C0) corresponding to the contribution of all imaged sarcomeric A-bands. However, SHG-AIPs are different between the center of the sarcomere (including the M line region of the sarcomere) and the hemi filaments (crossed-bridge regions of myosin thick filaments) as illustrated for myofibrils (compare thumbnails B1, C1 and B2, C2 of Fig. 3 D). This result well agrees with the simulation corresponding to a laser beam focused either at the center of the sarcomere (Fig. 2 A) and at the center of the hemi A-band (Fig. 2 B). Half angles between the two spots in thumbnails B0, B1 and C1 of Fig. 3 D are about 25°±1 which is close to the theoretical value 25.5° considering N=4 (Fig. 2 A). When the laser beam is focused at the center of the hemi sarcomere, SHG-AIP is either quite annular for bundle of myofibrils (Fig. 3 D, thumbnail B2) or centered spot for isolated myofibril (Fig. 3 D, thumbnail C2) which is well predicted by the theoretical simulation of Fig. 2 B considering respectively N=4 and N=2.

FIGURE 3. Experimental SHG-AIPs from healthy xenopus gastrocnemius muscle. SHG image from (A) thick muscular tissue with transversal xz (bottom) and yz (right) sections, (B) bundle of myofibrils, (C) single myofibril. (D) corresponding SHG-AIPs. Note that each thumbnail is labeled by the letter of the corresponding figure followed by a number localizing the ROI in the figure. Thumbnails A0, B0, C0 represent SHG-AIPs of the entire SHG image. Thumbnails B1, C1 represent the average SHG-AIP from the center of all A-bands of respectively bundle of myofibrils (B) and single myofibril (C). Thumbnails B2, C2 represent the average SHG-AIP from the remaining part of all sarcomeres of respectively bundle of myofibrils (B) and single myofibril (C). Full angular width of SHG-AIP in both x and y direction is 66° for (A) and 72° for (B) and (C). SHG-AIPs are in arbitrary units with increasing intensity from *blue* to *red*. Scale bars are 10 μm for (A) and 2 μm for (B) and (C).
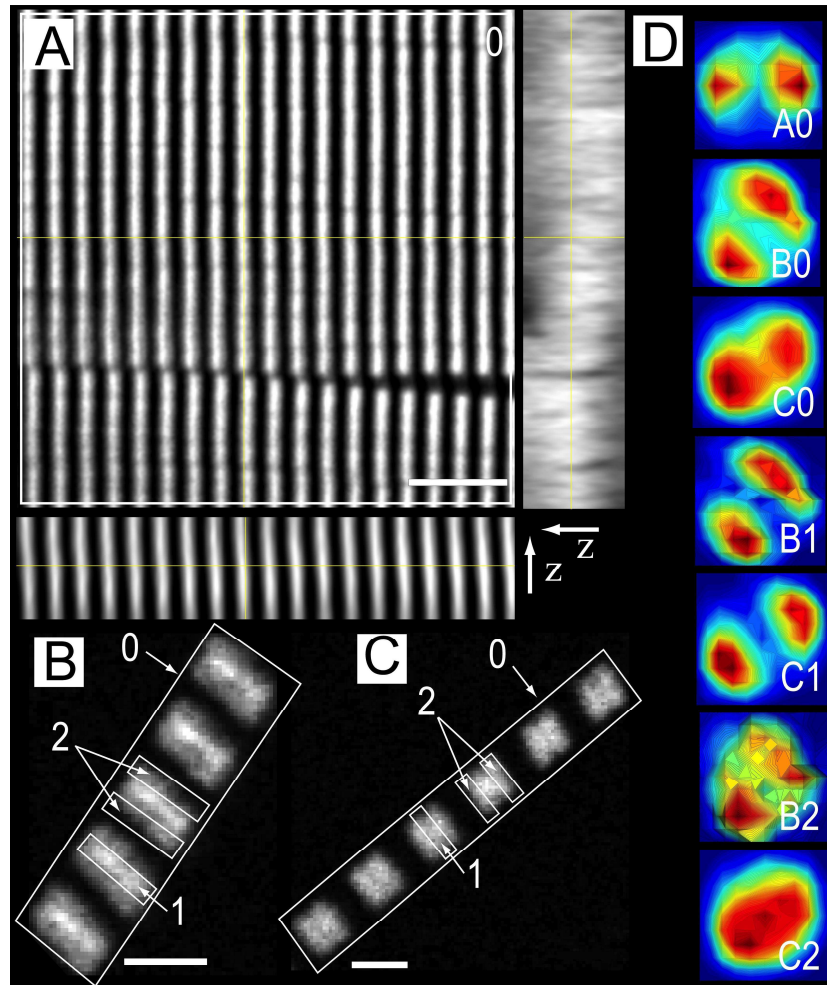
FIGURE 3. Experimental SHG-AIPs from healthy xenopus gastrocnemius muscle. SHG image from (A) thick muscular tissue with transversal xz (bottom) and yz (right) sections, (B) bundle of myofibrils, (C) single myofibril. (D) corresponding SHG-AIPs. Note that each thumbnail is labeled by the letter of the corresponding figure followed by a number localizing the ROI in the figure. Thumbnails A0, B0, C0 represent SHG-AIPs of the entire SHG image. Thumbnails B1, C1 represent the average SHG-AIP from the center of all A-bands of respectively bundle of myofibrils (B) and single myofibril (C). Thumbnails B2, C2 represent the average SHG-AIP from the remaining part of all sarcomeres of respectively bundle of myofibrils (B) and single myofibril (C). Full angular width of SHG-AIP in both x and y direction is 66° for (A) and 72° for (B) and (C). SHG-AIPs are in arbitrary units with increasing intensity from *blue* to *red*. Scale bars are $10 \ \mu m$ for (A) and $2 \ \mu m$ for (B) and (C).

For spontaneous post mortem highly proteolysed muscle tissue, SHG images and experimental SHG-AIPs are shown in Fig. 4 *A*. SHG intensity profiles (Fig. 4 *A*) are characterized by a bright sarcomeric double-band SHG-IP along the direction of the myofibril main axis in agreement with our previous results (25). Transversal views (Fig. 4 *A*) show disorganized myofibrils with misaligned sarcomeres (xz section, bottom) such that individual myofibrils can be resolved (yz section, right). SHG-AIPs measured from the entire field and from large ROIs of the SHG image (n = 40 ROIs from 10 xy fields) are all one centered spot as illustrated in Fig. 4 *B* (thumbnails *A0-A2*). As expected for such disorganized tissue, SHG-AIPs from localized ROIs (within the large ROIs) exhibit much more variability suggesting

that the centering of SHG-AIPs obtained from large ROIs is the result of the average of SHG-AIPs from several localized ROIs. It appears that mapping the spatial 3D myofibrillar organization from SHG-AIPs is complex from such highly proteolysed tissue. Nevertheless, for selective ROIs, SHG-AIPs (Fig. 4 *B*, thumbnails *A3-A6*) can be easily explained based on the theoretical analysis. For example, we found that myofibril displacement is either along x direction for ROIs 3-4 (compare Fig. 4 *B*, thumbnails *A3* and *A4* with Fig. 2, *C* and *D)* and along y direction for ROIs 5-6 (compare Fig. 4 *B*, thumbnails *A5*, *A6* with Fig. 2, *F* and *G)*. In contrast to highly proteolysed tissue, mild proteolysed muscle tissue provides a better understanding of the local 3D organization of myofibrils since a good correlation between experimental and theoretical SHG-AIPs can be easily obtained in that case as illustrated in Fig. S2.
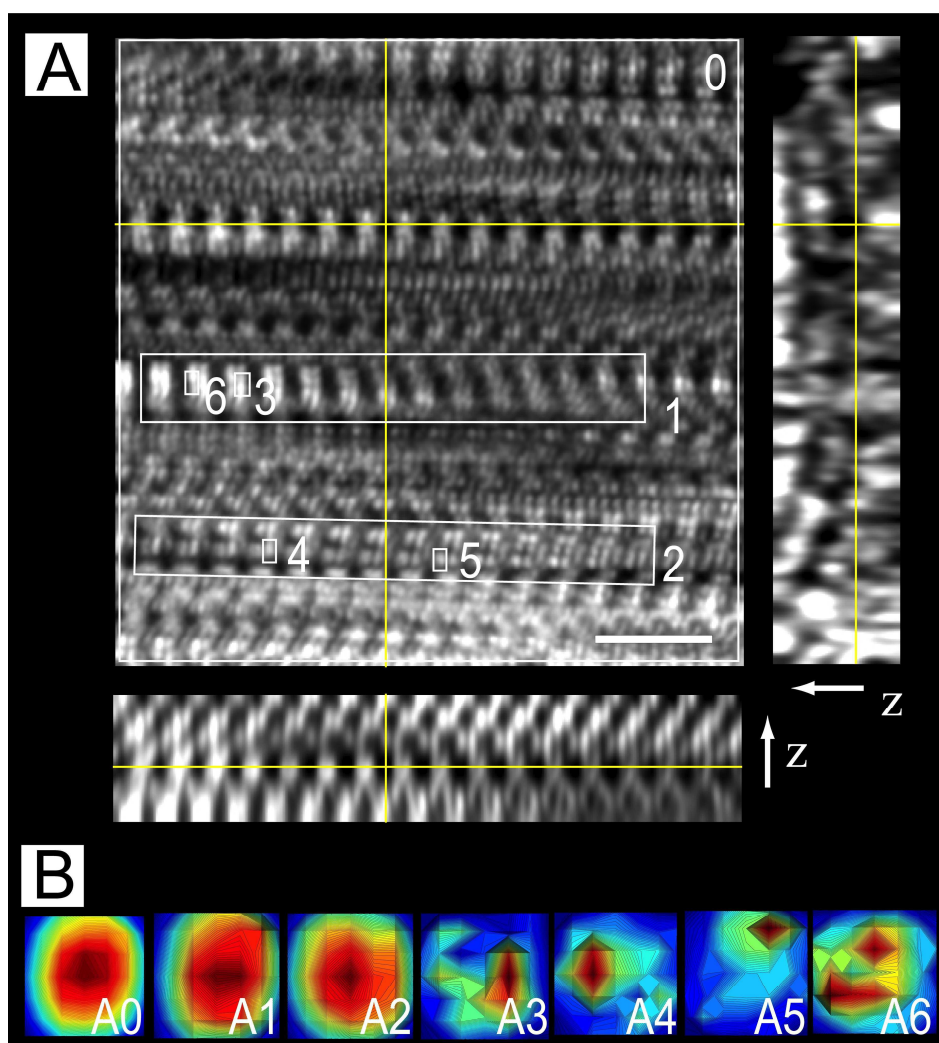

FIGURE 4. Experimental SHG-AIPs from proteolysed xenopus gastrocnemius muscle. SHG image from (A) thick slice of muscular tissue with transversal xz (bottom) and yz (right) sections, (B) corresponding SHG-AIPs. Note that each thumbnail is labeled by the letter of the corresponding figure followed by a number localizing the ROI in the figure. Note also that ROIs A0-A2 are large ROIs and A3-A6 are small ROIs. Full angular width of SHG-AIPs in both x and y direction is 66°. SHG-AIPs are in arbitrary units with increasing intensity from *blue* to *red*. Scale bar is $10 \, \mu m$.

We then used SHG-AIP to characterize muscle proteolysis from mouse model of Duchenne muscular dystrophy (mdx). Muscular dystrophies are a group of genetic diseases characterized by muscle weakness. The pathogenesis of Duchenne muscular dystrophy is frequently studied in the dystrophic mdx mouse model (29) and is characterized by muscle proteolysis and necrosis triggered by intracellular elevation of free calcium and oxidative stress (30-32). Experimental SHG images and SHG-AIPs of mdx mouse muscles are shown in Fig. 5. SHG image is characterized by a predominant bright single-band sarcomeric SHG-IP and less frequent vernier-like sarcomere irregularities as previously described by Friedrich et al. (33). Based on intensity profile analysis method (4), we have estimated that sarcomere irregularities correspond to double-band sarcomeric SHG-IP and their percentage significantly increases from 5% ±2 (n = 30 random fields) in control BL10 to 16 % ±3 (n = 30 random fields, p < 0.001, student T-test) in mdx muscles. Single-band SHG-IP was found to reliably segregate BL10 from mdx muscles (ROC AUC 0.82, 95% confidence interval from 0.71 to 0.92, P value < 0.001) as shown in figure 5 D. In mdx muscles, SHG-AIPs measured from large ROIs are illustrated in Fig. 5 *A* (ROIs 1-3). These large ROIs are chosen in regions with either single-band (ROI 1) or double-band (ROIs 2 and 3) sarcomeric SHG-IP. SHG-AIPs exhibit as expected, either two spots or one centered spot (Fig. 5 *B*). SHG-AIP quantification was undertaken in the same random fields as for SHG-IP. Predominant SHG-AIP pattern was found to be two spots (78%±5, p < 0.001, student T-test) in BL10 muscles and one spot in mdx muscles (85%±4, p < 0.001, student T-test). Two spots or one spot SHG-AIP was found to reliably segregate BL10 from mdx muscles (ROC AUC 0.97, 95% confidence interval from 0.93 to 1, P value < 0.001) as shown in figure 5 D. Moreover, ROC analysis curve suggested that SHG-AIP method is more sensitive than SHG-IP method to segregate BL10 from mdx muscles. Compared to large ROIs, SHG-AIPs from small ROIs exhibit more heterogeneity even in regions with single-band SHG-IP. In these latter, mdx skeletal muscle tissue appears to be strongly deformed. This distortion induces localized myofibrillar misalignment either along x or -x directions as observed in the xz sections (Fig. 5 *C*). Corresponding SHG-AIPs (Fig. 5 *B*) are asymmetrical spots emitted in a direction that is opposite to the myofibrillar misalignment, in agreement with the results reported in Fig. S2. SHG-AIPs from two different myofibrils (arrowheads in Fig. 5 *A*) with double-band sarcomeric SHG-IP were also analyzed to determine their local displacement. SHG-AIPs (Fig. 5 *B*) suggest that myofibrillar displacement is mainly along x direction for one myofibril (ROIs *A*11-*A*14) and is more complex for the other (ROIs *A*7- *A*10). From the above results, we conclude that SHG-AIP is a powerful tool to determine the local 3D myofibrillar disorganization of pathological muscular tissue.
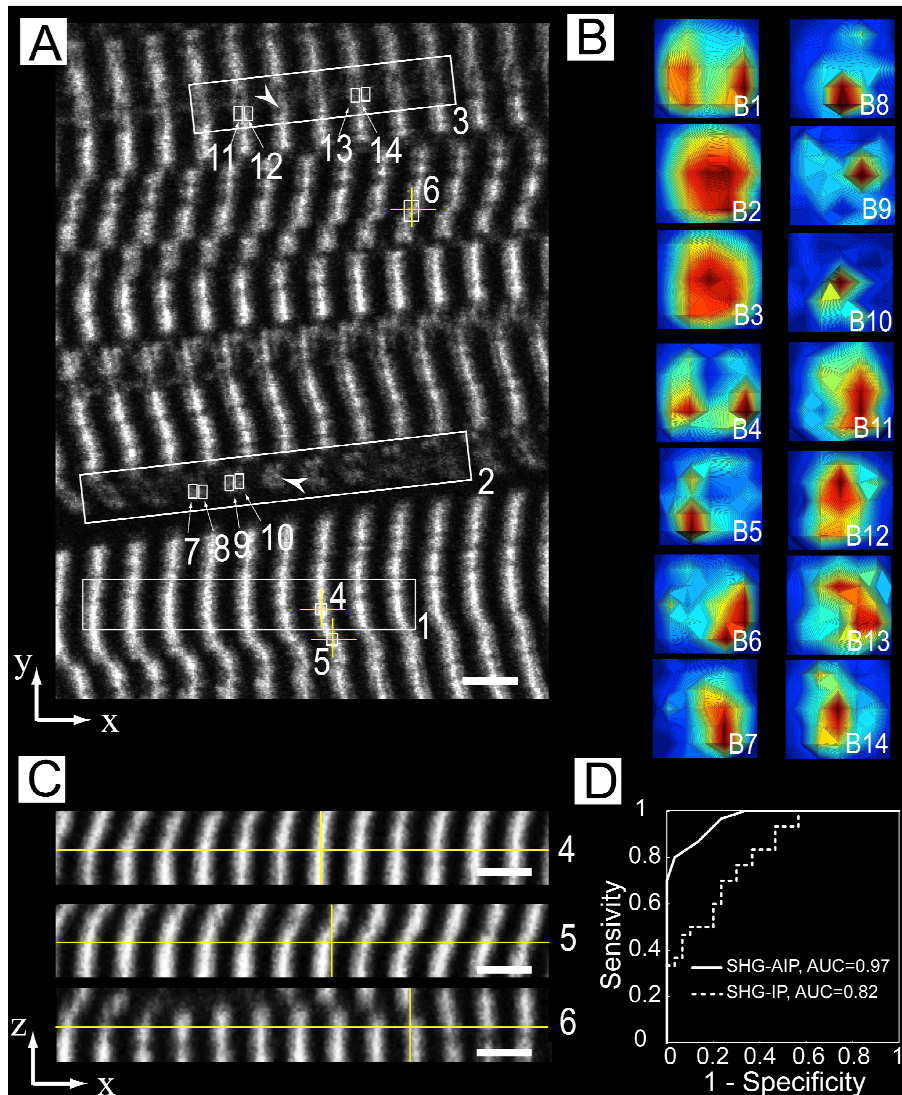
FIGURE 5. Experimental SHG-AIPs from mdx mouse muscle and ROC curve analysis. (A) SHG image from a thick slice of muscular tissue. Note that ROIs 1-3 are large ROIs and 4-14 are small ROIs. The sarcomeric SHG intensity pattern feature of ROIs 1, 4-6 is single-band and that of ROIs 2, 3, 7-14 is double-band. Note also that ROIs 7-10 and ROIs 11-14 correspond to two different myofibrils (*arrowheads*). (B) Corresponding SHG-AIPs. Note that each thumbnail is labeled by the letter of the corresponding figure followed by a number localizing the ROI in the figure. Note also that thumbnails B7-B10 suggest complex myofibrillar displacement while thumbnails B10-B14 suggest more simple myofibrillar displacement mainly along x direction. Full angular width of SHG-AIP in both x and y direction is 60°. SHG-AIPs are in arbitrary units with increasing intensity from *blue* to *red*. (C) Transversal xz views. Each xz view is obtained at the center (yellow cross) of the corresponding ROI (labeled with the same number) in (A). (D) Discrimination of control BL10 and Dystrophic mdx muscles using ROC curve (Receiver operating characteristic curve) and area under curve (ROC AUC) analysis. Continuous curve represents percentage of ROIs with two spots SHG-AIP in each random field analyzed. Dotted curve represents percentage of ROIs with single-band sarcomeric SHG-IP in the same random fields. Note that AUC for each curve is indicated in the figure. 95% confidence intervals are 0.93 to 1 and 0.71 to 0.92 respectively for SHG-AIP and SHG-IP ROC AUC. Data are from 12 animals (6 BL10

and 6 mdx), 30 random fields (60×60 μm) in each group, 8 homogeneously distributed ROIs in the entire field were analyzed (see Material and Methods). Scale bar is $5\,\mu m$.

DISCUSSION

In this report, we have shown that myosin thick filament polarity inversion occurring at the center of the sarcomere is responsible to scattering of harmonic light in muscular tissue. Directions of scattering are determined by the local 3D organization of a few myofibrils in the focusing volume. We have calculated SHG-AIP in muscle tissue in order to gain insight into the organization of myofibrils both in physiological and non-physiological conditions. We have also reported for the first time experimental SHG-AIPs in muscle tissue obtained by modification of the experimental setup. We found that experimental SHG-AIP of healthy muscle is characterized by two symmetrical spots emitted along the myofibril main axis in agreement with the theoretical simulation. Moreover, the variability of SHG-AIP observed for proteolysed muscle tissue put forward that SHG-AIP technique is very sensitive to probe the local 3D myofibrillar displacements.

Theoretical simulation is based on a simplified structural model of myofibrils that is sufficient to explain the observed experimental results. In this model, myofibrils have a rectangular shape and thick filaments are supposed to be well aligned and centered in each sarcomere. The M-band at the center of each sarcomere and the sarcoplasmic reticulum are also neglected as their volume is small compared to the one of the PSF. Taking into account these parameters modifies the overall SHG intensity but not the shape of the SHG-AIP which is controlled by the modulation wave vector $\mathbf{Q}$ associated with myofibrillar displacement. Modulus of $\mathbf{Q}$ is also defined by the size of the PSF. It ranges from $\sim \pi / w_{xy} (= 6.5 \; \mu m^{-1})$ for healthy muscle with polarity transition only along x direction to $\sim \pi / w_{z} (= 1.3 \; \mu m^{-1})$ for proteolysed muscle with polarity transition only along z direction. Theoretical simulation shows that SHG intensity is built only over a small excitation volume $(1.81)^3 \times w_{xy}^2 \times w_z$ of the order of $3\,\mu m^3$ in our experimental conditions. Therefore, SHG-AIP provides structural information within this volume that corresponds to 4-8 myofibrils of average diameter $1\,\mu m$ (34). We found this simple model sufficient to explain the observed experimental results. As SHG process is a result of constructive interferences between harmonic waves, we show that high SHG intensity can be obtained in biological tissue only for non zero wave vectors $\mathbf{Q}$ as expressed by Eq. 2. For the particular case of myosin muscle tissue, we also showed that polarity transition occurring at the center of the A-band drastically affects $\mathbf{Q}$ values and therefore SHG-AIPs. For healthy tissue, polarity transition at the center of the sarcomere results in a better constructive interferences process and an over intensity (Figs. 2 A, 3A) compared to the center of the hemi sarcomere (Figs. 2 B, 3A) where polarity is homogeneous as previously reported (22). In contrast to thick tissue, integrated SHG intensity for isolated myofibrils is lower at the center of the sarcomere when compared to the center of the hemi sarcomere both in the experimental results (Fig. 3 C) and in the simulation (Fig. 2, A and B, N=2). For N=1, integrated SHG intensity is 11 at the center of the sarcomere and 14 at the center of the hemi sarcomere (data not shown). This implies that sarcomeric SHG-IP is double-band in healthy myofibril and therefore this pattern cannot be a marker of proteolysis in isolated myofibrils in contrast to our previous suggestion (24). The over intensity observed at the center of the hemi sarcomere for isolated myofibril is explained as follows. SHG-AIP is more centered for N=2 (and N=1) than for N=4 or 6. Consequently, at low θ value,

constructive and destructive interferences between harmonic photons are generated respectively at the center of the hemi sarcomere and at the center of the sarcomere as previously explained (22). As a result, higher SHG intensity is obtained at the center of the hemi sarcomere than at the center of the sarcomere for N=1 or 2.

We have previously shown that sarcomeric SHG-IP analysis enables discrimination between healthy and proteolysed muscle tissue (25). This method classifies sarcomeric SHG-IP as single-band or double-band respectively for healthy and proteolysed muscle tissues. In the present study, ROC curve analysis suggests that SHG-AIP (ROC AUC = 0.97) and SHG-IP (ROC AUC = 0.82) are very sensitive methods to discriminate between healthy and disease mdx muscles. In a previous study, evaluation of muscle damage based on single sarcomere pattern parameter alone (either fraction of non hyper contracted sarcomeres or their mean length was found insufficient (ROC AUC = 0.75) for clear discrimination of mild or moderate mdx muscle from control sample (26). In that study, combination of three sarcomere pattern parameters was necessary to achieve sensitivity (ROC AUC =1) greater than that of SHG-AIP method described herein. From this study, we conclude that SHG-AIP with two symmetrical spots is a signature of healthy myofibrils while SHG-AIP with one centered spot in mdx muscle is a signature of myofibrillar disorder. Therefore SHG-AIP analysis could be a useful tool to map myofibrillar alignment in muscle tissues during development, maturation and regeneration and gain access to their biological cues.

The pathogenesis of Duchenne muscular dystrophy is characterized by muscle proteolysis and necrosis triggered by intracellular elevation of free calcium and oxidative stress (30-32). The increase of double-band sarcomeric SHG-IP that we observed in mdx mouse is in agreement with our previous report showing that oxidative stress and muscle proteolysis affect sarcomeric SHG-IP (24,25,35). The myofibrillar misalignment revealed by SHG-AIP also reflects this proteolysis even in myofibrils that are presumed to be "healthy" considering sarcomeric SHG-IP analysis. However the consequence of this myofibrillar misalignment on the E-C coupling awaits further studies. We anticipate that SHG-AIP will be a useful tool to probe structural modification affecting the E-C coupling. This latter is the mechanism that links transverse tubules (T-tubules) depolarization to Ca^{2+} release from the sarcoplasmic reticulum that triggers, in turn, muscle contraction. T-tubules are orderly invaginations of surface membrane along the Z-line regions, with regular spacing ($\sim 2\ \mu m$) along myofibrils. This widely distributed, highly organized T-tubule system is essential for rapid electric excitation and coordinated contraction of each contractile unit throughout the entire cytoplasm. Alteration of this T-tubule system and E-C coupling by myofibrillar displacements is expected to reduce muscle contraction. In heart diseases such as heart failure and ischemia, myofibril disorganization and T-tubule disorganization or loss have been linked to decreased contractility (36,37). In skeletal muscle, mutations in sarcomeric proteins are known to cause around 20 different diseases however the pathophysiology of the gene defects remains remarkably obscure (38). Structural myofibrillar disorganization are observed in several human skeletal muscle diseases including Duchenne muscular dystrophy (39). Genetic studies from mouse have shown that mutation of the cytoskeleton intermediate filament desmin gene result in myofibrillar misalignment, reduced muscle tension, compromised endurance performance and more susceptibility to damage due to eccentric exercise (40,41). We anticipate that SHG-AIP will be of paramount to study, in thick tissue, the spatial correlation between myofibrillar disorganization and E-C disruption occurring in physiological adaptation and in disease.

CONCLUSION

In this work, we report second harmonic scattering of light by muscular tissue. We show that angular emission of SHG light is driven by the local 3D myofibrillar organization in the excitation volume. Compared to SHG intensity pattern, we also show that SHG-AIP provides extra hints to map at sub-optical resolution the local 3D myofibrillar organization of both healthy and pathological muscle tissue.

REFERENCES

1.   Campagnola, P. J. and L. M. Loew. 2003. Second-harmonic imaging microscopy for visualizing biomolecular arrays in cells, tissues and organisms. Nat Biotechnol 21:1356-1360.

2.   Zipfel, W. R., R. M. Williams, and W. W. Webb. 2003. Nonlinear magic: multiphoton microscopy in the biosciences. Nat Biotechnol 21:1369-1377.

3.   Lacomb, R., O. Nadiarnykh, S. S. Townsend, and P. J. Campagnola. 2008. Phase Matching considerations in Second Harmonic Generation from tissues: Effects on emission directionality, conversion efficiency and observed morphology. Opt Commun 281:1823-1832.

4.   Han, M., G. Giese, and J. F. Bille. 2005. Second harmonic generation imaging of collagen fibrils in cornea and sclera. Optics Express 13:5791-5797.

5.   Williams, R. M., W. R. Zipfel, and W. W. Webb. 2005. Interpreting second-harmonic generation images of collagen I fibrils. Biophysical Journal 88:1377-1386.

6.   Theodossiou, T. A., C. Thrasivoulou, C. Ekwobi, and D. L. Becker. 2006. Second harmonic generation confocal microscopy of collagen type I from rat tendon cryosections. Biophysical Journal 91:4665-4677.

7.   Pfeffer, C. P., B. R. Olsen, and F. Legare. 2007. Second harmonic generation imaging of fascia within thick tissue block. Optics Express 15:7296-7302.

8.   Legare, F., C. Pfeffer, and B. R. Olsen. 2007. The role of backscattering in SHG tissue imaging. Biophysical Journal 93:1312-1320.

9.   Fu, Y., H. Wang, R. Shi, and J.-X. Cheng. 2007. Second harmonic and sum frequency generation imaging of fibrous astroglial filaments in ex vivo spinal tissues. Biophysical Journal 92:3251-3259.

10.   Wang, B.-G., A. Eitner, J. Lindenau, and K.-J. Halbhuber. 2008. High-resolution two-photon excitation microscopy of ocular tissues in porcine eye. Lasers in Surgery and Medicine 40:247-256.

11.   Han, X., R. M. Burke, M. L. Zettel, P. Tang, and E. B. Brown. 2008. Second harmonic properties of tumor collagen: determining the structural relationship between reactive stroma and healthy stroma. Optics Express 16:1846-1859.

12.   Hsueh, C.-M., W. Lo, W.-L. Chen, V. A. Hovhannisyan, G.-Y. Liu, S.-S. Wang, H.-Y. Tan, and C.-Y. Dong. 2009. Structural Characterization of Edematous Corneas by Forward and Backward Second Harmonic Generation Imaging. Biophysical Journal 97:1198-1205.

13.   Campagnola, P. J. and C.-Y. Dong. 2011. Second harmonic generation microscopy: principles and applications to disease diagnosis. Laser & Photonics Reviews 5:13-26.

14.   Freund, I. 1968. Nonlinear diffraction. Physical Review Letters 21:1404-1406.

15.   Freund, I., M. Deutsch, and A. Sprecher. 1986. Connective-tissue polarity - optical 2nd-harmonic microscopy, crossed-beam summation, and small-angle scattering in rat-tail tendon. Biophysical Journal 50:693-712.

16.   Dolino, G., Lajzerow.J, and M. Vallade. 1970. Second-harmonic light scattering by domains in ferroelectric triglycine sulfate. Physical Review B 2:2194-&.

17.   Rouède, D., Y. Le Grand, P. Rabiller, and C. Scherf. 2000. Study of antiparallel pyroelectric twins in KLiSO4 by second-harmonic scattering. Optics Communications 178:225-232.

18.   Mertz, J. and L. Moreaux. 2001. Second-harmonic generation by focused excitation of inhomogeneously distributed scatterers. Optics Communications 196:325-330.

19.   Tian, L., J. L. Qu, Z. Y. Guo, Y. Jin, Y. Y. Meng, and X. Y. Deng. 2010. Microscopic second-harmonic generation emission direction in fibrillous collagen type I by quasi-phase-matching theory. Journal of Applied Physics 108.

20.   Tian, L., H. J. Wei, Y. Jin, H. P. Liu, Z. Y. Guo, and X. Y. Deng. 2011. Backward emission angle of microscopic second-harmonic generation from crystallized type I collagen fiber. J. Biomed. Opt. 16.

21.   Mertz, J. 2010. Introduction to optical microscopy. Greenwood Village: Roberts & Company Publishers.

22.   Rouède, D., G. Recher, J. J. Bellanger, M. T. Lavault, E. Schaub, and F. Tiaho. 2011. Modeling of Supramolecular Centrosymmetry Effect on Sarcomeric SHG Intensity Pattern of Skeletal Muscles. Biophysical Journal 101:494-503.

23.   Gouy, L. G. 1890. Sur une propriété nouvelle des ondes lumineuses. C. R. Acad. Sci. Paris 110:1251-1253.

24.   Recher, G., D. Rouède, C. Tascon, L. A. D'Amico, and F. Tiaho. 2011. Double-band sarcomeric SHG pattern induced by adult skeletal muscles alteration during myofibrils preparation. Journal of Microscopy 241:207-211.

25.   Recher, G., D. Rouède, P. Richard, A. Simon, J.-J. Bellanger, and F. Tiaho. 2009. Three distinct sarcomeric patterns of skeletal muscle revealed by SHG and TPEF Microscopy. Opt. Express 17:19763-19777.

26.   Plotnikov, S. V., A. M. Kenny, S. J. Walsh, B. Zubrowski, C. Joseph, V. L. Scranton, G. A. Kuchel, D. Dauser, M. Xu, C. C. Pilbeam, D. J. Adams, R. P. Dougherty, P. J. Campagnola, and W. A. Mohler. 2008. Measurement of muscle disease by quantitative second-harmonic generation imaging. J Biomed Opt 13:044018.

27.   Mertz, J. 2001. Nonlinear microscopy. C. R. Acad. Sci. Ser. IV-Phys. Astrophys. 2:1153-1160.

28.   Bendat, J. S. 2010. Random Data: Analysis and Measurement Procedures. Hoboken, New Jersey: John Wiley and Sons. 640 p.

29.   Bulfield, G., W. G. Siller, P. A. Wight, and K. J. Moore. 1984. X chromosome-linked muscular dystrophy (mdx) in the mouse. Proc Natl Acad Sci U S A 81:1189-1192.

30.   Turner, P. R., T. Westwood, C. M. Regen, and R. A. Steinhardt. 1988. Increased protein degradation results from elevated free calcium levels found in muscle from mdx mice. Nature 335:735-738.

31.   Franco, A., Jr. and J. B. Lansman. 1990. Calcium entry through stretch-inactivated ion channels in mdx myotubes. Nature 344:670-673.

32.   Tidball, J. G. and M. Wehling-Henricks. 2007. The role of free radicals in the pathophysiology of muscular dystrophy. J Appl Physiol 102:1677-1686.

33.   Friedrich, O., M. Both, C. Weber, S. Schurmann, M. D. H. Teichmann, F. von Wegner, R. H. A. Fink, M. Vogel, J. S. Chamberlain, and C. Garbe. 2010. Microarchitecture Is

Severely Compromised but Motor Protein Function Is Preserved in Dystrophic mdx Skeletal Muscle. Biophysical Journal 98:606-616.

34.   Colomo, F., N. Piroddi, C. Poggesi, G. T. Kronnie, and C. Tesi. 1997. Active and passive forces of isolated myofibrils from cardiac and fast skeletal muscle of the frog. Journal of Physiology-London 500:535-548.

35.   Recher, G., D. Rouède, E. Schaub, and F. Tiaho. 2011. Skeletal muscle sarcomeric SHG patterns photo-conversion by femtosecond infrared laser. Biomed. Opt. Express 2:374-384.

36.   Song, L. S., E. A. Sobie, S. McCulle, W. J. Lederer, C. W. Balke, and H. Cheng. 2006. Orphaned ryanodine receptors in the failing heart. Proc Natl Acad Sci U S A 103:4305-4310.

37.   Lyon, A. R., K. T. MacLeod, Y. Zhang, E. Garcia, G. K. Kanda, M. J. Lab, Y. E. Korchev, S. E. Harding, and J. Gorelik. 2009. Loss of T-tubules and other changes to surface topography in ventricular myocytes from failing human and rat heart. Proc Natl Acad Sci U S A 106:6854-6859.

38.   Laing, N. G. and K. J. Nowak. 2005. When contractile proteins go bad: the sarcomere and skeletal muscle disease. Bioessays 27:809-822.

39.   Dubowitz, V. and C. A. Sewry. 2007. Muscle Biopsy: A Practical Approach, Third Edition. London.

40.   Lovering, R. M., A. O'Neill, J. M. Muriel, B. L. Prosser, J. Strong, and R. J. Bloch. 2011. Physiology, structure, and susceptibility to injury of skeletal muscle in mice lacking keratin 19-based and desmin-based intermediate filaments. American journal of physiology 300:C803-813.

41.   Li, Z., M. Mericskay, O. Agbulut, G. Butler-Browne, L. Carlsson, L. E. Thornell, C. Babinet, and D. Paulin. 1997. Desmin is essential for the tensile strength and integrity of myofibrils but not for myogenic commitment, differentiation, and fusion of skeletal muscle. J Cell Biol 139:129-144.